

Manganese Oxide/Carbon Yolk–Shell Nanorod Anodes for High Capacity Lithium Batteries

Zhengyang Cai,^{†,§} Lin Xu,^{†,‡,§} Mengyu Yan,[†] Chunhua Han,[†] Liang He,^{*,†} Kalele Mulonda Hercule,[†] Chaojiang Niu,[†] Zefan Yuan,[†] Wangwang Xu,[†] Longbing Qu,[†] Kangning Zhao,[†] and Liqiang Mai^{*,†}

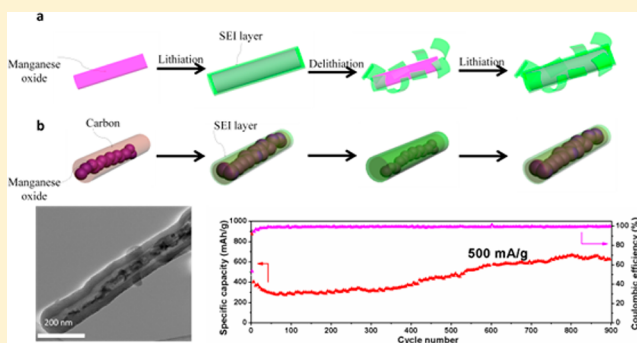
[†]State Key Laboratory of Advanced Technology for Materials Synthesis and Processing, WUT-Harvard Joint Nano Key Laboratory, Wuhan University of Technology, Wuhan 430070, China

[‡]Department of Chemistry and Chemical Biology, Harvard University, Cambridge, Massachusetts 02138, United States

S Supporting Information

ABSTRACT: Transition metal oxides have attracted much interest for their high energy density in lithium batteries. However, the fast capacity fading and the low power density still limit their practical implementation. In order to overcome these challenges, one-dimensional yolk–shell nanorods have been successfully constructed using manganese oxide as an example through a facile two-step sol–gel coating method. Dopamine and tetraethoxysilane are used as precursors to obtain uniform polymer coating and silica layer followed by converting into carbon shell and hollow space, respectively. As anode material for lithium batteries, the manganese oxide/carbon yolk–shell nanorod electrode has a reversible capacity of 660 mAh/g for initial cycle at 100 mA/g and exhibits excellent cyclability with a capacity of 634 mAh/g after 900 cycles at a current density of 500 mA/g. An enhanced capacity is observed during the long-term cycling process, which may be attributed to the structural integrity, the stability of solid electrolyte interphase layer, and the electrochemical actuation of the yolk–shell nanorod structure. The results demonstrate that the manganese oxide is well utilized with the one-dimensional yolk–shell structure, which represents an efficient way to realize excellent performance for practical applications.

KEYWORDS: Yolk–shell nanorod, manganese oxide, long-life, volume change, anode material



Recently, lithium batteries have been widely developed to meet the demands of a variety of energy applications, such as grid storage, hybrid electric vehicles, and portable electronic devices because of their high energy density and long lifespan.^{1–5} As is known to all, electrode materials play an important role in battery performance. Commercially used graphite anode materials deliver a specific capacity of 372 mAh/g.^{6,7} To meet the enormous demands of energy consumptions, a material with higher capacity is required.^{8–12} Compared with conventional graphite materials, transition metal oxide materials based on conversion reaction mechanism such as cobalt oxides, copper oxides, iron oxides, etc., have shown high reversible capacity.^{13–16} Among them, Mn_3O_4 has attracted the most attention for its natural abundance, no toxicity, cost effectiveness, and high theoretical capacity, making it a promising anode material for high performance lithium batteries.^{17–19} However, poor rate performance and rapid capacity decays during cycling still exist for Mn_3O_4 . These drawbacks may be ascribed to the following: (1) extremely low electrical conductivity ($\sim 10^{-7}$ – 10^{-8} S/cm)²⁰ and (2) significant volume change during the lithium insertion/extraction process in manganese oxide, which leads to the degradation of the mechanical integrity and the instability of the solid

electrolyte interphase (SEI).^{6,8} In spite of the disappointing results, great efforts have been made to optimize the performance of manganese oxide electrode by carbon coating, morphology control, and selective growth method.^{20–27}

Presently, yolk–shell nanostructure, a new class of architecture, has attracted great attention in various applications, especially in the field of lithium batteries.²⁸ The yolk–shell structure in combination with carbon shell can provide a new strategy to solve some drawbacks existing in anode materials, such as the large volume change, low conductivity, and poor cycling performance. Recently, some efforts have been made to explore this kind of structure. Cui and co-workers²⁹ have designed a Si/void/C nanoparticle electrode by using SiO_2 as the sacrificial template, it delivers a capacity as high as 2000 mAh/g after 50 cycles, which is several times larger than that of Si/C nanoparticle electrode. Moreover, the yolk–shell structure is also suitable for transition metal oxides. Lou and co-workers³⁰ have successfully developed a general route for the synthesis of ternary ZnMn_2O_4 ball-in-ball hollow structure,

Received: November 18, 2014

Published: December 9, 2014

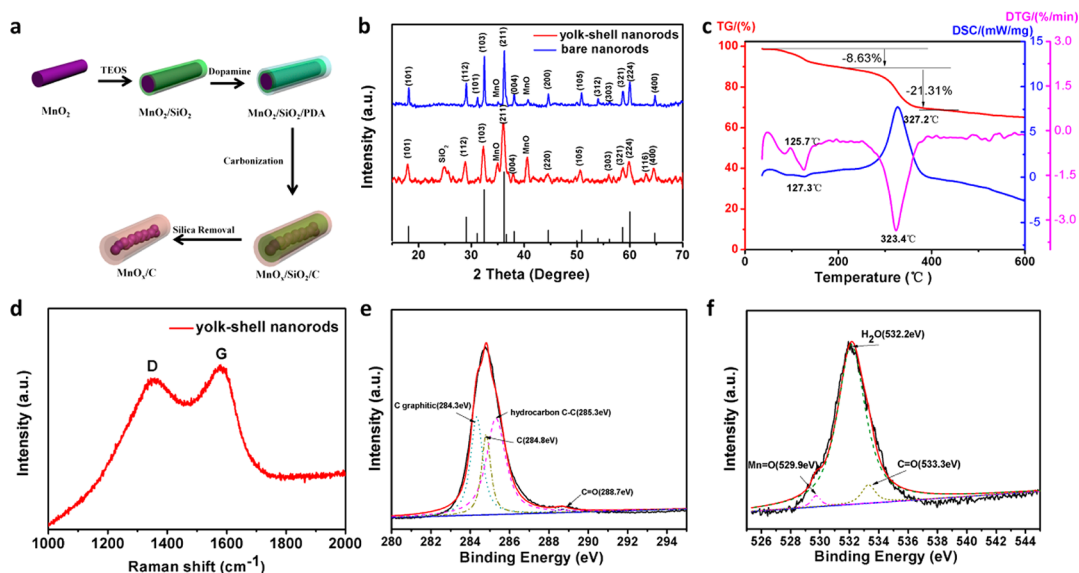


Figure 1. (a) Schematic illustration of formation processes of the manganese oxide/carbon yolk–shell nanorods. (b) XRD patterns of manganese oxide/carbon yolk–shell nanorods (red line), bare manganese oxide nanorods (blue line), and the standard sample hausmannite Mn_3O_4 card (black line). (c) TGA (red line), DSC (blue line), and DTG (purple line) curves of the manganese oxide/carbon yolk–shell nanorods under air atmosphere at a rate of $10^\circ\text{C}/\text{min}$. (d) Raman spectrum for synthesized manganese oxide/carbon yolk–shell nanorods. (e, f) XPS spectra of manganese oxide/carbon yolk–shell nanorods: (e) high resolution of C_{1s} and (f) high resolution of O_{1s} .

which shows significantly enhanced electrochemical performance when used as anode material for lithium batteries. Despite the great successes, previous works mainly focused on zero dimensional yolk–shell nanoparticles.^{31–34} Recently, novel one-dimensional nanostructure has shown great potential in energy storage, nanoelectronics fields, etc.^{35–40} Therefore, one-dimensional yolk–shell structure with more active reaction sites and shorter diffusion paths will be of great benefit for lithium batteries. Nevertheless, this unique structure has seldom been reported,^{41–43} partly the reason being that it is difficult to make two uniform coating layers around the structure, especially for transition metal oxide.

In this Letter, taking manganese oxides as an example, we designed and synthesized novel yolk–shell nanorods using sol–gel method with both high specific capacity and long cycle capability for lithium batteries. The synthesis procedure is mainly composed of four steps as illustrated in Figure 1a.⁴⁴ In this structure, the core is manganese oxide nanorod consisting of small particles, while the shell is carbon, which allows lithium ion to pass through, and the void space between manganese oxide and carbon can buffer the volume change during the lithium ion insertion/extraction process.

The yolk–shell nanorod structure possesses several unique properties as anode material: (1) the one-dimensional yolk–shell nanorod materials have more active reaction sites caused by higher Brunauer–Emmett–Teller (BET) surface area of $30.9\text{ m}^2/\text{g}$, shorter diffusion paths for both lithium ions and electrons providing faster redox reactions;⁴⁵ (2) the internal stress induced by large volume changes during the lithium insertion/extraction process can be buffered through the available void spaces around, and thus pulverization and collapse can be prevented and a stable structure is obtained; (3) since the relationship between the stability of SEI and the electrochemical performance of lithium batteries has been reported,⁴⁶ the SEI formed around the carbon shell at the first cycle can keep stable because the expanded manganese oxide core may not disturb the carbon shell;^{29,47} (4) good

conductivity can be realized for the composite material because the carbon shell is a good electronic conductor. All of these facts make manganese oxide/carbon yolk–shell a promising anode material for practical applications.

The crystal structure of the as-prepared sample was characterized by X-ray diffraction (XRD). All the diffraction peaks of the precursor sample can be well assigned to high purity $\beta\text{-MnO}_2$ with tetragonal structure (JCPDS Card No. 81-2261, space group $P42/mnm$) (Figure S1, Supporting Information). As shown in Figure 1b, the manganese oxide/carbon yolk–shell nanorods are mainly composed of hausmannite Mn_3O_4 with tetragonal structure (JCPDS Card No. 89-4837, space group $I41/amd$, $a = b = 5.76\text{ \AA}$, $c = 9.46\text{ \AA}$, $\alpha = \beta = \gamma = 90^\circ$). The presence of MnO is indicated by the broad peaks at 34.9° and 40.6° . This phase reveals that the $\text{MnO}_2/\text{SiO}_2/\text{poly dopamine}$ (poly-DPA) nanorods underwent a phase transition in the N_2 atmosphere during the carbonization procedure. The broad peak located at 25.0° can be assigned to silica and the small amount of silica may come from the silica template. For comparison, bare manganese oxide nanorods prepared by similar method without the additions of tetraethoxysilane (TEOS) and DPA have shown similar peaks with manganese oxide/carbon yolk–shell nanorods (Figure 1b). Then thermogravimetric analysis (TG) was carried out to determine the carbon content of the materials (Figure 1c). A mass loss of about 8.63% is observed below 200°C on the TG curve, and an endothermic processes around 127°C in the DSC curve may correspond to the loss of free water, physically adsorbed water, and the reaction of residual $\text{Na}_2\text{SiO}_3 \cdot n\text{H}_2\text{O}$. An intensive exothermic peak at 327.2°C result from the burning of carbon shell, which led to a mass loss of about 21.3%.

In order to further figure out the poly-DPA decomposed product, the Raman spectrum is given in Figure 1d. The two peaks located at 1324 and 1602 cm^{-1} can be assigned to the D band and G band of carbon, respectively. The intensity ratio of G band and D band (I_G/I_D) is measured to be 1.052 indicating that the shell is amorphous carbon. Moreover, in the high

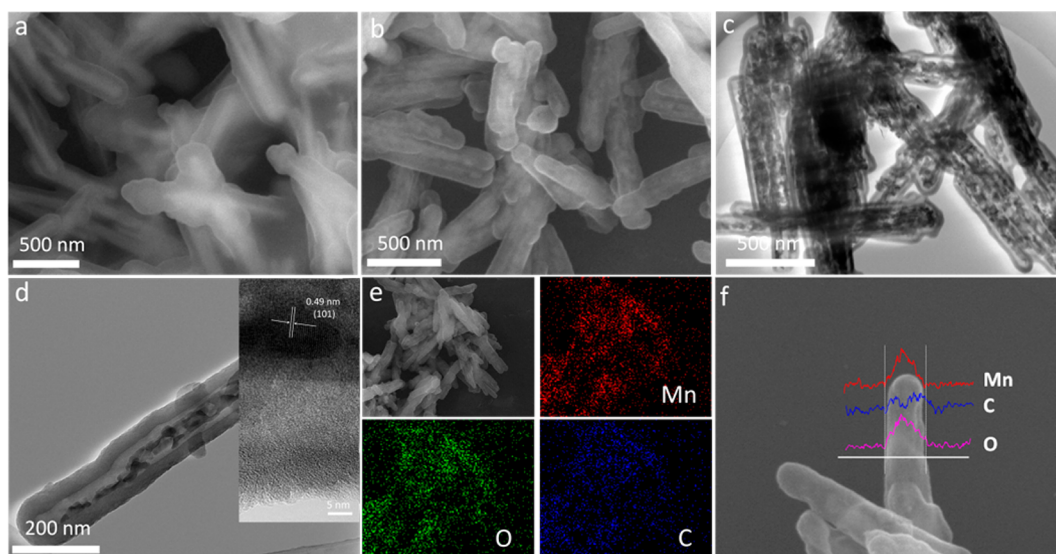


Figure 2. (a) FESEM image of manganese oxide/silica/polydopamine nanorods. (b,c) FESEM image (b) and TEM image (c) of manganese oxide/carbon yolk-shell nanorods. (d) TEM image of a single manganese oxide/carbon yolk-shell nanorod; the inset shows the HRTEM image of the nanorod with a scale bar of 5 nm. (e) EDS elemental mapping of Mn, O, and C, respectively. (f) FESEM image and corresponding EDS line scanning profiles of Mn (red line), C (blue line), and O (purple line) recorded along the white line.

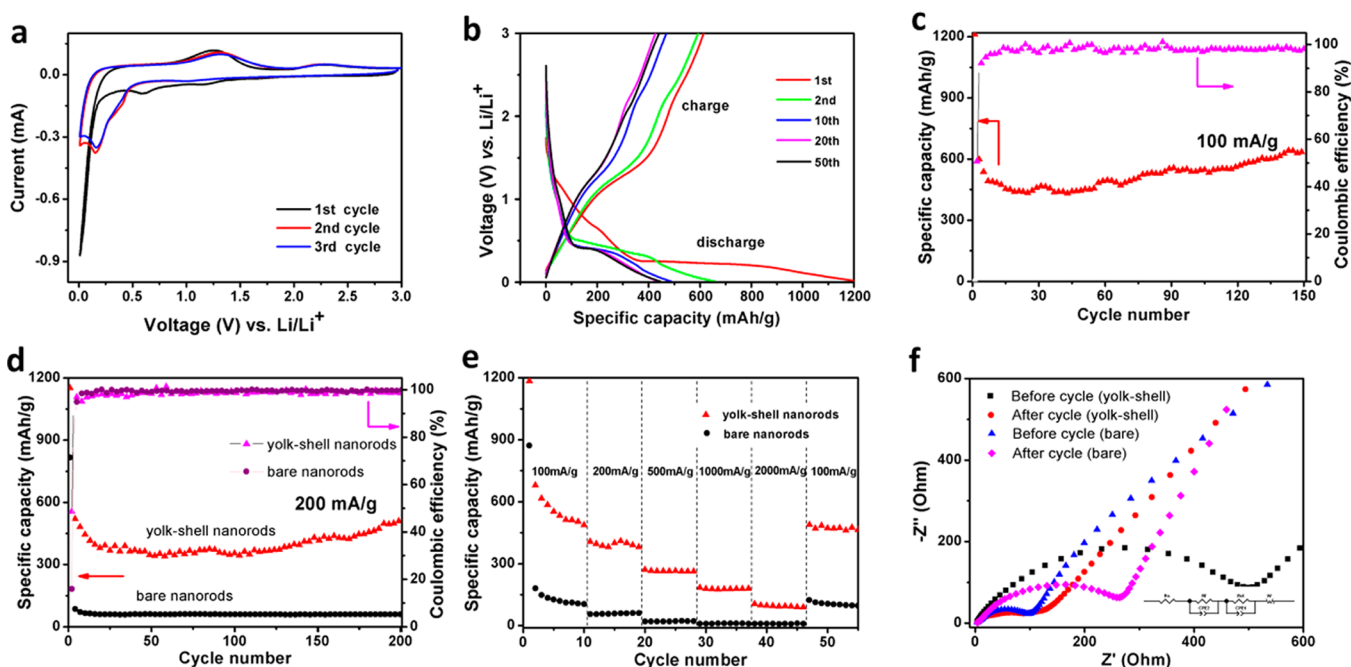


Figure 3. (a) CV curves of yolk-shell nanorods at a scan rate of 0.1 mV/s in the potential range from 3.0 to 0.01 V vs Li/Li⁺. (b) Charge-discharge curves of yolk-shell nanorods at 100 mA/g for different cycles. (c) Cycling performance of yolk-shell nanorods at 100 mA/g. (d) Cycling performance of yolk-shell nanorods and bare nanorods at 200 mA/g. (e) Rate performance of yolk-shell nanorods. (f) AC Impedance plots for yolk-shell nanorods and bare nanorods before and after rate performance.

resolution spectrum of C_{1s} (Figure 1e), the sample mainly contains graphite carbon (284.3 eV) and hydrocarbon (285.3 eV). A broad peak observed at 288.7 eV can be attributed to the C=O bond, which is consistent with that in the high resolution spectrum of O_{1s} (Figure 1f). These results, combined with comparison data (Figure S2, Supporting Information), demonstrate that the poly-DPA converts to amorphous carbon during the calcining procedure.

To investigate the functions of TEOS and DPA in controllable synthesis and provide the detailed information on the manganese oxide/carbon yolk-shell nanorods, field

emission scanning electron microscopy (FESEM) and transmission electron microscopy (TEM) images are provided. The uniform MnO₂ nanorods with an average diameter of about 90 nm and a length of about 2.5 μm were prepared by a simple hydrothermal method (Figure S3a, Supporting Information). MnO₂/SiO₂ nanorods obtained by the sol-gel process show a smooth surface, and the thickness of the silica shell is about 15 nm as shown in the magnified FESEM image (Figure S3b, Supporting Information). Then a DPA self-polymerization process leads to the formation of MnO₂/SiO₂/poly-DPA nanorods (Figure 2a) with a diameter of about 180 nm,

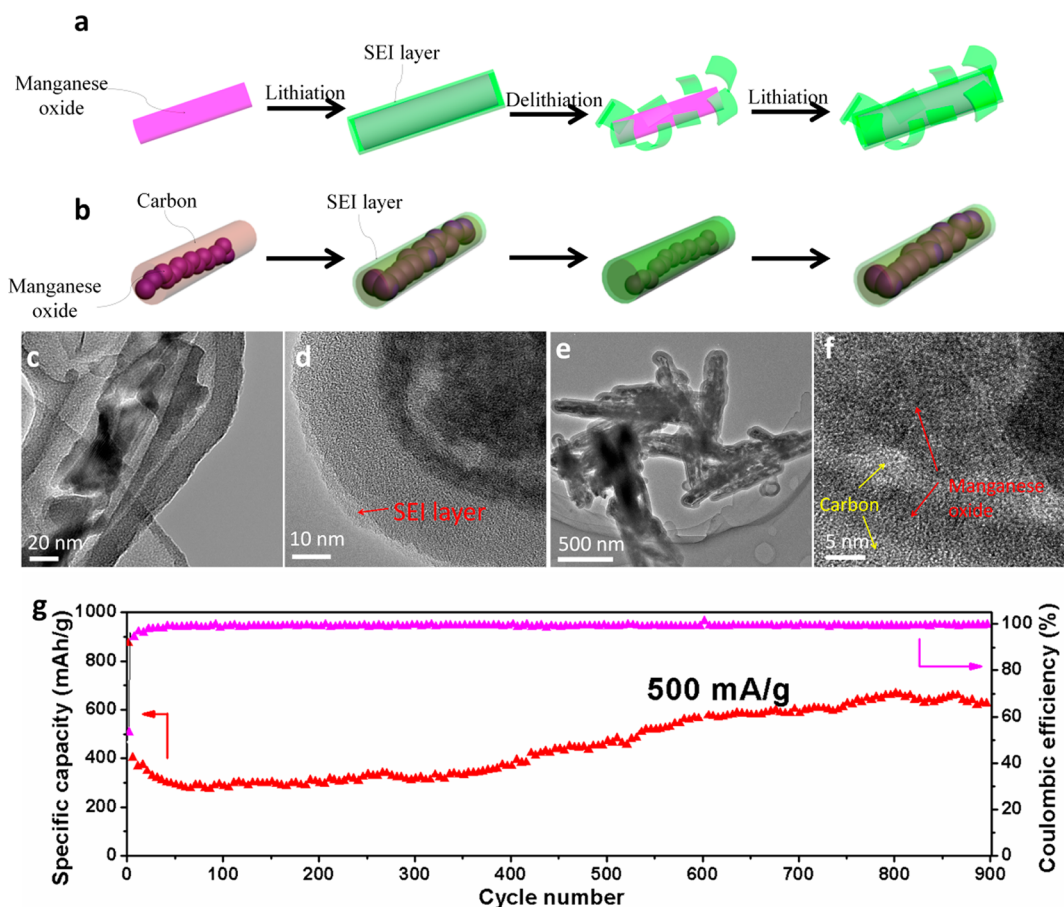


Figure 4. (a,b) Three-dimensional view of (a) the bare manganese oxide nanorod and (b) the manganese oxide/carbon yolk-shell nanorod during lithiation and delithiation processes. The conductive carbon can block the electrolyte and prevent the SEI formation inside the nanorod while allowing the lithium ions to transport throughout the carbon. (c–f) TEM images of manganese oxide/carbon yolk-shell nanorod before (c) and after (d–f) electrochemical cycling for 500 cycles. (d) The SEI layer formed around the carbon shell with a thickness of several nanometers. (e) The yolk-shell nanorods can maintain integrity even after cycling. (f) The distribution of manganese oxide inside the nanorod. (g) Long-life cycling performance of manganese oxide/carbon yolk-shell nanorod electrode at 500 mA/g.

revealing the presence of about 40 nm thick poly-DPA layer. It is noted that the uniform, smooth, and coherent coating of poly-DPA may be attributed to the fact that DPA can attach to many kinds of surfaces leading to a strong interaction with the substrates.⁴⁸

Moreover, a rough surface was observed for manganese oxide/silica/carbon nanorods after the carbonization process at 500 °C under the N₂ atmosphere (Figure S3c, Supporting Information). The elemental distribution of the material was further characterized by energy dispersive spectroscopic (EDS) mapping (Figure S4, Supporting Information). After an etching process conducted in NaOH solution to remove the silica layer, the manganese oxide/carbon yolk-shell nanorods were prepared (Figure 2b). It is clear that the manganese oxide nanorods fracture into nanoparticles during the sintering process, and there is no significant change in size during the procedure. Detailed information on the structure is observed in TEM images (Figure 2c,d). It provides the evidence that the nanorods possess a yolk-shell structure and the contrast between the hollow and solid parts is obviously observed. From the high magnification TEM image, we can see that, the thickness of the carbon shell is about 32 nm, while the average thickness of the core is about 36 nm. Moreover, the high resolution transmission electron microscopy (HRTEM) image (Figure 2d, inset) displays a lattice fringe with d-spacing of 0.49

nm, corresponding to the (101) plane of tetragonal crystal shown in XRD pattern. The amorphous carbon layer can also be observed in the image. Furthermore, EDS elemental mapping and line scanning (Figure 2e,f) clearly confirm the presence and distribution of Mn, O, and C elements and further demonstrate the yolk-shell nanostructure with a manganese oxide core and carbon shell. Particularly, the thick carbon coating can make the structure robust and stable,³⁰ which may be beneficial to the cycling performance when used as anode material for lithium batteries. Then bare manganese oxide nanorods were prepared for comparison (Figure S3d, Supporting Information).

Electrochemical performances were characterized for the manganese oxide/carbon yolk-shell nanorod electrode.⁴⁹ It is noted that the capacity is calculated based on the total mass of the materials containing carbon shell and manganese oxide core and the capacity of the carbon shell is very low as shown in Figure S5, Supporting Information. Cyclic voltammetry was tested for 3 cycles at a sweep rate of 0.1 mV/s in the potential range from 3.0 to 0.01 V vs Li/Li⁺ at room temperature. As depicted in Figure 3a, in the first cathodic polarization process, a broad peak centered at about 1.15 V and an intense peak at low potential are attributed to the reduction of manganese oxide to metallic manganese and the formation of Li₂O,^{20,50} another cathodic peak located at about 0.75 V corresponds to

the decomposition of electrolyte and formation of SEI layer on the surface of electrode materials.²¹ The peak located at about 1.3 V in the first anodic sweep corresponds to the oxidation of manganese. For the next scans, the main cathodic peak shifts to about 0.25 V, indicating an irreversible phase change. Moreover, the curve of the third scan is similar to that of the second one, implying a highly reversible property. The similar profiles of the bare manganese nanorods demonstrate that similar reactions occur during the charge/discharge process (Figure S7a, Supporting Information). Noteworthy, the presence of MnO phase may not seriously affect the electrochemical property as a whole (Figure S6, Supporting Information). The Mn₃O₄ phase conducts the electrochemical conversion reaction: $\text{Mn}_3\text{O}_4 + 8\text{Li}^+ + 8\text{e}^- \rightarrow 3\text{Mn} + 4\text{Li}_2\text{O}$, with a theoretical capacity of 936 mAh/g based on the equation $C = nN_A(e/M)$. Similarly, the MnO phase delivers the electrochemical conversion reaction $\text{MnO} + 2\text{Li}^+ + 2\text{e}^- \rightarrow \text{Mn} + \text{Li}_2\text{O}$, with a theoretical capacity of 755 mAh/g. The difference between the two manganese oxide phases is the number of transferred electrons, which just leads to a small decrease on the theoretical capacity and has no effect on the electrochemical mechanism.

The voltage profiles of different cycles for yolk-shell nanorod electrode at a current density of 100 mA/g are shown in Figure 3b. The potential plateau in range of 0.2–0.55 V corresponds to the lithiation process while that in 1.2–1.5 V to the delithiation. In the second, 10th, 20th, and 50th cycles, the discharge capacities are 660, 483, 440, and 448 mAh/g, respectively, much higher than that of bare manganese oxide electrode (Figure S7b, Supporting Information). Moreover, the potential plateau at around 0.4 V keeps stable even after 50 cycles, indicating superior and stable cycling performance. In addition, the electrode delivers a capacity of 649 mAh/g even after 150 cycles, and the Coulombic efficiency of the electrode is maintained around 98% in the subsequent cycles (Figure 3c).

The cycling performance of the manganese oxide/carbon yolk-shell nanorod electrode and pure manganese oxide nanorod electrode at current density of 200 mA/g are shown in Figure 3d. A much better cycling stability can be observed for the yolk-shell nanorod electrode. After 20 cycles, it delivers a discharge capacity of 381 mAh/g, whereas that of bare manganese oxide is just 62 mAh/g. Even after 200 cycles, the yolk-shell nanorod electrode can still reach 509 mAh/g in capacity with slight increase. However, a discharge capacity of only 61 mAh/g can be obtained for bare manganese oxide electrode in the same condition. In addition, after the first several cycles, the Coulombic efficiency can remain at around 98.3%, indicating good reversibility of the manganese oxide/carbon yolk-shell nanorods. Also, we provide the average capacity based on three batteries for the cycling performance (Figure S8, Supporting Information). Furthermore, in rate performance tests, the electrode is tested at different charge and discharge rates ranging from 100 to 2000 mA/g (Figure 3e); it exhibited the capacities of 487, 382, 263, 179, 91, and 474 mAh/g, respectively. Remarkably, the capacity is retained at 474 mAh/g when the current density returns to 100 mA/g, manifesting excellent rate performance compared to that of bare manganese oxide nanorods (109 mAh/g).

An excellent cycling performance is an important factor for promising anode materials. In this case, the manganese oxide/carbon yolk-shell nanorod electrode is cycled at various current densities to investigate the long-life performance. The electrode exhibits a capacity of 932 mAh/g at 200 mA/g after

400 cycles and 837 mAh/g at 300 mA/g after 600 cycles (Figure S9, Supporting Information). Even at a high current density of 500 mA/g, the discharge capacity of the manganese oxide/carbon yolk-shell nanorod electrode is 289 mAh/g after 100 cycles. Afterward the capacity increases gradually until around 600 cycles and then keeps stable for the subsequent cycles and finally reaches 634 mAh/g after 900 cycles. The retentive capacity is measured to be 72.5% relative to the initial one (Figure 4g). Compared with previously reported manganese oxide/carbonous hybrid materials (Table S1, Supporting Information), the manganese oxide/carbon yolk-shell nanorod electrode shows enhanced reversible capacity after long-term cycles. Notably, the increased capacity of manganese oxide/carbon yolk-shell nanorods is also widely observed for many transition metal oxides. This phenomenon may be attributed to the growth of an electrochemically gel-like polymer layer, which can enhance lithium ion storage.^{14,51} For another reason, as can be seen from Figure S10, Supporting Information, the proportion of the total active materials on the internal surface of the carbon shell increases and the size of the manganese oxide particles reduces, which can be ascribed to the electrochemically driven reconstruction of the manganese oxide.⁵² The phenomenon may enhance the electrochemical activity and result in an improved capacity.

The above results have shown that the present yolk-shell nanorod electrode exhibits excellent electrochemical properties. Just as illustrated in Figure 4b, the void space around the manganese oxide allows it to expand without deforming the overall morphology during lithiation/delithiation process, so the SEI layer formed outside the nanorod is not ruptured during cycling and keeps thin (Figure 4c,d).⁴⁷ However, as shown in Figure 4a, the bare nanorod suffers a repeated breaking and formation of SEI layer during cycling leading to thick SEI layers (Figure S11a,b, Supporting Information). In addition, the electrochemical impedance spectra (EIS) are also provided to certify the enhanced capacity of yolk-shell nanorods. In the equivalent circuit, R_s represents the resistance of the electrolyte, R_{ct} represents the charge transfer resistance, and R_f represents the resistance of the SEI film. CPE and Z_w are the double layer capacitance and the Warburg impedance, respectively. All the curves exhibit a semicircle in the high frequency region followed by a straight line in the low frequency region (Figure 3f). The yolk-shell nanorod electrode shows an initial resistance of 465 Ω and cycled resistance of 89 Ω . The decrease of charge transfer resistance indicates the activation and improved kinetics of the reaction. Moreover, the values of R_{ct} at the first, 200th, and 500th cycles also show similar tendency (Figure S12, Supporting Information). However, for bare manganese oxide nanorod electrode, the R_{ct} increases. These opposite behaviors can further demonstrate that the electrochemical activation that occurred during the charge/discharge cycles can help enhance the conversion reaction and improve the electrochemical activity for manganese oxide/carbon yolk-shell nanorods,⁵² and this is evidenced by the strong adhesion of manganese core and carbon shell after cycles (Figure 4f). Furthermore, the void space between manganese oxide core and carbon shell can buffer the volume change and keep the integrity of the structure (Figures 4e and S11c,d, Supporting Information). Thus, high capacity and long life are realized for the manganese oxide/carbon yolk-shell nanorod electrode as anode.

In summary, the yolk-shell nanorods with manganese oxide core and carbon shell have been constructed using a facile sol-

gel method. The one-dimensional manganese oxide/carbon yolk-shell nanorods with carbon around can buffer the volume change, improve the electronic conductivity, enhance the stability of the electrode, and prevent the SEI layer from breaking during cycles even at a high rate. It is demonstrated that the manganese oxide/carbon yolk-shell nanorod electrode exhibits excellent electrochemical performance in terms of reversible specific capacity and cycling stability, especially where a capacity of about 634 mAh/g after 900 cycles has been realized. This novel structure can be further extended for other one-dimensional materials, and it is of great potential for next-generation energy storage and other applications.

■ ASSOCIATED CONTENT

Supporting Information

Additional information and figures. This material is available free of charge via the Internet at <http://pubs.acs.org>.

■ AUTHOR INFORMATION

Corresponding Authors

*E-mail: mlq518@whut.edu.cn.

*E-mail: hel@whut.edu.cn.

Author Contributions

[§]These authors contributed equally to this work.

Notes

The authors declare no competing financial interest.

■ ACKNOWLEDGMENTS

This work is supported by the National Natural Basic Research Program of China (2013CB934103 and 2012CB933003), the National Science Fund for Distinguished Young Scholars (51425204), the International Science and Technology Cooperation Program of China (2013DFAS0840), the National Natural Science Foundation of China (51272197 and 51302203), the Hubei Science Fund for Distinguished Young Scholars (2014CFA035), the Fundamental Research Funds for the Central Universities (2013-ZD-7 and 2014-yb-002), and the Students Innovation and Entrepreneurship Training Program (136601001 and 20131049701002). We are grateful to Prof. C. M. Lieber of Harvard University and Prof. D. Y. Zhao of Fudan University for strong support and stimulating discussions.

■ REFERENCES

- (1) Tarascon, J.-M.; Armand, M. *Nature* **2001**, *414* (6861), 359–367.
- (2) Dunn, B.; Kamath, H.; Tarascon, J.-M. *Science* **2011**, *334* (6058), 928–935.
- (3) Kang, B.; Ceder, G. *Nature* **2009**, *458* (7235), 190–193.
- (4) Goodenough, J. B.; Park, K.-S. *J. Am. Chem. Soc.* **2013**, *135* (4), 1167–1176.
- (5) Zhao, Y.; Xu, L.; Mai, L.; Han, C.; An, Q.; Xu, X.; Liu, X.; Zhang, Q. *Proc. Natl. Acad. Sci. U.S.A.* **2012**, *109* (48), 19569–19574.
- (6) Cabana, J.; Monconduit, L.; Larcher, D.; Palacin, M. R. *Adv. Mater.* **2010**, *22* (35), E170–E192.
- (7) Ji, J.; Ji, H.; Zhang, L. L.; Zhao, X.; Bai, X.; Fan, X.; Zhang, F.; Ruoff, R. S. *Adv. Mater.* **2013**, *25* (33), 4673–4677.
- (8) Jiang, J.; Li, Y.; Liu, J.; Huang, X.; Yuan, C.; Lou, X. W. D. *Adv. Mater.* **2012**, *24* (38), 5166–5180.
- (9) Mahmood, N.; Zhang, C.; Yin, H.; Hou, Y. *J. Mater. Chem. A* **2014**, *2* (1), 15–32.
- (10) Chan, C. K.; Peng, H.; Liu, G.; McIlwrath, K.; Zhang, X. F.; Huggins, R. A.; Cui, Y. *Nat. Nanotechnol.* **2008**, *3* (1), 31–35.
- (11) Mahmood, N.; Zhang, C.; Hou, Y. *Small* **2013**, *9* (8), 1321–1328.
- (12) Xu, J.; Wu, H.; Wang, F.; Xia, Y.; Zheng, G. *Adv. Energy Mater.* **2013**, *3* (3), 286–289.
- (13) Lu, X.; Zhai, T.; Zhang, X.; Shen, Y.; Yuan, L.; Hu, B.; Gong, L.; Chen, J.; Gao, Y.; Zhou, J. *Adv. Mater.* **2012**, *24* (7), 938–944.
- (14) Grugeon, S.; Laruelle, S.; Dupont, L.; Tarascon, J.-M. *Solid State Sci.* **2003**, *5* (6), 895–904.
- (15) Zeng, Y.; Hao, R.; Xing, B.; Hou, Y.; Xu, Z. *Chem. Commun.* **2010**, *46* (22), 3920–3922.
- (16) Wu, H.; Xu, M.; Wu, H.; Xu, J.; Wang, Y.; Peng, Z.; Zheng, G. *J. Mater. Chem.* **2012**, *22* (37), 19821–19825.
- (17) Luo, W.; Hu, X.; Sun, Y.; Huang, Y. *ACS Appl. Mater. Interface* **2013**, *5* (6), 1997–2003.
- (18) Wang, Y.; Wang, Y.; Jia, D.; Peng, Z.; Xia, Y.; Zheng, G. *Nano Lett.* **2014**, *14* (2), 1080–1084.
- (19) Kim, J.-S.; Kim, K.; Cho, W.; Shin, W. H.; Kanno, R.; Choi, J. *W. Nano Lett.* **2012**, *12* (12), 6358–6365.
- (20) Wang, H.; Cui, L.-F.; Yang, Y.; Sanchez Casalongue, H.; Robinson, J. T.; Liang, Y.; Cui, Y.; Dai, H. *J. Am. Chem. Soc.* **2010**, *132* (40), 13978–13980.
- (21) Wang, C.; Yin, L.; Xiang, D.; Qi, Y. *ACS Appl. Mater. Interface* **2012**, *4* (3), 1636–1642.
- (22) Gao, J.; Lowe, M. A.; Abruna, H. D. *Chem. Mater.* **2011**, *23* (13), 3223–3227.
- (23) Hao, Q.; Wang, J.; Xu, C. *J. Mater. Chem. A* **2014**, *2* (1), 87–93.
- (24) Li, Y.; Huang, S.; Jin, J.; Cai, Y.; Tan, H.; Wang, H.-E.; Van Tendeloo, G.; Su, B. L. *Nanoscale* **2014**, *6*, 6819–6827.
- (25) Guo, J.; Liu, Q.; Wang, C.; Zachariah, M. R. *Adv. Funct. Mater.* **2012**, *22* (4), 803–811.
- (26) Chang, L.; Mai, L.; Xu, X.; An, Q.; Zhao, Y.; Wang, D.; Feng, X. *RSC Adv.* **2013**, *3* (6), 1947–1952.
- (27) Jiang, H.; Hu, Y.; Guo, S.; Yan, C.; Lee, P. S.; Li, C. *ACS Nano* **2014**, *8* (6), 6038–6046.
- (28) Lai, X.; Li, J.; Korgel, B. A.; Dong, Z.; Li, Z.; Su, F.; Du, J.; Wang, D. *Angew. Chem.* **2011**, *123* (12), 2790–2793.
- (29) Liu, N.; Wu, H.; McDowell, M. T.; Yao, Y.; Wang, C.; Cui, Y. *Nano Lett.* **2012**, *12* (6), 3315–3321.
- (30) Zhang, G.; Yu, L.; Wu, H. B.; Hoster, H. E.; Lou, X. W. D. *Adv. Mater.* **2012**, *24* (34), 4609–4613.
- (31) Liu, J.; Qiao, S. Z.; Chen, J. S.; Lou, X. W. D.; Xing, X.; Lu, G. Q. *M. Chem. Commun.* **2011**, *47* (47), 12578–12591.
- (32) Chen, S.; Gordin, M. L.; Yi, R.; Howlett, G.; Sohn, H.; Wang, D. *Phys. Chem. Chem. Phys.* **2012**, *14* (37), 12741–12745.
- (33) Liu, J.; Qiao, S. Z.; Budi Hartono, S.; Lu, G. Q. *M. Angew. Chem.* **2010**, *122* (29), 5101–5105.
- (34) Wang, J.; Li, W.; Wang, F.; Xia, Y.-Y.; Asiri, A. M.; Zhao, D. *Nanoscale* **2014**, *6*, 3217–3222.
- (35) (a) Kim, S.-K.; Day, R. W.; Cahoon, J. F.; Kempa, T. J.; Song, K.-D.; Park, H.-G.; Lieber, C. M. *Nano Lett.* **2012**, *12* (9), 4971–4976. (b) Mai, L.; Tian, X.; Xu, X.; Chang, L.; Xu, L. *Chem. Rev.* **2014**, *114* (23), 11828–11862.
- (36) Yan, H.; Choe, H. S.; Nam, S.; Hu, Y.; Das, S.; Klemic, J. F.; Ellenbogen, J. C.; Lieber, C. M. *Nature* **2011**, *470* (7333), 240–244.
- (37) Sun, B.; Chen, Z.; Kim, H.-S.; Ahn, H.; Wang, G. J. *Power Sources* **2011**, *196* (6), 3346–3349.
- (38) Mai, L.; Xu, L.; Han, C.; Xu, X.; Luo, Y.; Zhao, S.; Zhao, Y. *Nano Lett.* **2010**, *10* (11), 4750–4755.
- (39) Kempa, T. J.; Cahoon, J. F.; Kim, S.-K.; Day, R. W.; Bell, D. C.; Park, H.-G.; Lieber, C. M. *Proc. Natl. Acad. Sci. U.S.A.* **2012**, *109* (5), 1407–1412.
- (40) Jiang, X.; Tian, B.; Xiang, J.; Qian, F.; Zheng, G.; Wang, H.; Mai, L.; Lieber, C. M. *Proc. Natl. Acad. Sci. U.S.A.* **2011**, *108* (30), 12212–12216.
- (41) Yan, M.; Wang, F.; Han, C.; Ma, X.; Xu, X.; An, Q.; Xu, L.; Niu, C.; Zhao, Y.; Tian, X. *J. Am. Chem. Soc.* **2013**, *135* (48), 18176–18182.
- (42) Lou, X. W.; Yuan, C.; Archer, L. A. *Adv. Mater.* **2007**, *19* (20), 3328–3332.
- (43) Guan, C.; Wang, X.; Zhang, Q.; Fan, Z.; Zhang, H.; Fan, H. J. *Nano Lett.* **2014**, *14* (8), 4852–4858.

(44) Methods: MnO₂ nanorods were prepared by mixing MnSO₄·H₂O and (NH₄)₂S₂O₈ in deionized water followed by a hydrothermal method at 180 °C for 12 h. Then a stober sol–gel coating process was conducted, where dispersed MnO₂ nanorods were coated with a layer of silica to obtain MnO₂/silica nanorods using TEOS as precursor. Afterwards, the sample was dissolved in a mix solution containing 2 mg/mL DPA and 10 mM TRIS for 5 h to obtain MnO₂/silica/poly-DPA nanorods. Moreover, the precursors were carbonized at 500 °C for 2 h under a N₂ atmosphere to convert the poly-DPA into a carbon layer to produce MnO₂/silica/carbon nanorods. Finally, it is the silica removal process, where the silica layer can be etched away by a 1 M NaOH solution to yield the manganese oxide/carbon yolk–shell nanorods. (More details in Supporting Information.) Characterization: XRD measurements were performed by using a Bruker D8 Advance X-ray diffractometer with a nonmonochromated Cu Ka X-ray source. Raman spectra were acquired using a Renishaw RM-1000 laser Raman microscopy system. FESEM images were collected using a JEOL JSM-7100F at an acceleration voltage of 20 kV. TEM and HRTEM images were recorded using a JEOL JEM-2100F STEM/EDS microscope. EDS were recorded by using Oxford EDS IE250. XPS analysis was done on VG Multilab 2000. BET surface areas were measured using Tristar II 3020 instrument to measure the adsorption of nitrogen. TGA was performed using a Netzsch STA 449F3 simultaneous thermal analyzer at a heating rate of 10 °C/min in air.

(45) Lieber, C. M.; Wang, Z. L. *MRS Bull.* **2007**, *32* (02), 99–108.

(46) Wu, H.; Chan, G.; Choi, J. W.; Ryu, I.; Yao, Y.; McDowell, M. T.; Lee, S. W.; Jackson, A.; Yang, Y.; Hu, L. *Nat. Nanotechnol.* **2012**, *7* (5), 310–315.

(47) Liu, N.; Lu, Z.; Zhao, J.; McDowell, M. T.; Lee, H.-W.; Zhao, W.; Cui, Y. *Nat. Nanotechnol.* **2014**, *9* (3), 187–192.

(48) Lee, H.; Dellatore, S. M.; Miller, W. M.; Messersmith, P. B. *Science* **2007**, *318* (5849), 426–430.

(49) Electrochemical measurements: The electrochemical properties were characterized by means of 2016 coin cells using lithium metal foil as the anode. The electrodes were composed of 70% active material, 20% acetylene black, and 10% poly(tetrafluoroethylene) (PTFE) binder. The acetylene black is used as a dispersing agent and a conducting additive to ensure the successful grinding of the as-prepared powders to cut into pellets. A solution (1 M) of LiPF₆ in EC-DEC (1:1 vol/vol) was used as the electrolyte. The cells were assembled in an argon filled glovebox. Galvanostatic charge–discharge measurements were performed using a multichannel battery testing system (LAND CT2001A), and cyclic voltammetry (CV) and electrochemical impedance spectra (EIS) were performed using an Autolab Potentiostat Galvanostat. All the measurements were carried out at room temperature.

(50) Thackeray, M.; David, W.; Bruce, P.; Goodenough, J. *Mater. Res. Bull.* **1983**, *18* (4), 461–472.

(51) Laruelle, S.; Grugeon, S.; Poizot, P.; Dolle, M.; Dupont, L.; Tarascon, J. J. *Electrochem. Soc.* **2002**, *149* (5), A627–A634.

(52) Sun, Y.; Hu, X.; Luo, W.; Xia, F.; Huang, Y. *Adv. Funct. Mater.* **2013**, *23* (19), 2436–2444.